Quantification of the structure evolution in a garden soil over the course of two years

John Koestel[a,*], Steffen Schlüter[b]

[a] Swedish University of Agricultural Sciences, Department of Soil & Environment, P.O. Box 7014, SE-75007 Uppsala, Sweden
[b] Helmholtz-Centre for Environmental Research – UfZ, Department of Soil System Science, Theodor-Lieser-Str.4, D-06120 Halle, Germany

A B S T R A C T

In this proof-of-concept, we demonstrate the potential of quantifying the structural evolution in an individual soil sample with the help of X-ray imaging. The soil sample was acquired in summer 2013 after a manual seedbed preparation and scanned with X-ray CT on six occasions during the following two years. After each imaging session, the soil sample was re-installed into the field. We focused on analyzing the evolution of soil morphologic measures that are thought to be fundamental to air and water flow in soil. We also quantified deformation of the soil matrix during the experiment. Our results illustrate the effects of several biotic and abiotic processes on the evolution of soil structure. A well-connected inter-aggregate pore network after seedbed preparation was replaced by a sparser network of larger biopores. Macro-faunal burrowing activity generally increased morphological measures associated with larger air and hydraulic conductivity as well as a better aeration. Soil settling and the growth of a dandelion tap-root acted in the opposite direction. Soil settling and compaction continued during the entire experimental period, but was restricted to soil depths below 20 mm. Other noteworthy observations that appear worth investigating in follow-up experiments were i.) the strong variation in the critical pore diameter, which could explain the commonly noted large temporal variability of saturated hydraulic conductivity, ii) the much greater extent of lateral compaction due to tap root growth than macro-faunal burrowing, and iii.) the short life-span of large biopores. We conclude that the approach presented here shows great potential for quantifying soil structural dynamics pertaining to individual structure-forming and degrading processes under field conditions. This kind of data could also prove very useful for constructing and testing 'next-generation' models that link a dynamic description of soil structure to various processes and functions in the soil-plant system.

1. Introduction

The architecture of the macropore network is fundamental for several physical properties and associated soil functions. Examples are the near-saturated and saturated hydraulic conductivity or the air permeability at field capacity. The better connected the macropores are in a soil, the larger the soil's capacity to transport air and water quickly (Jarvis et al., 2016). One related soil function is the soil infiltration capacity which influences susceptibility to overland flow and erosion (Assouline, 2013). Moreover, the soil macrostructure also determines which regions within the soil volume are well supplied with atmospheric oxygen and which are not (Ben-Noah and Friedman, 2018). The former are located close to macropores that are connected to the soil surface and the latter are not, which means that periods of anaerobic conditions are more likely to prevail (Parry et al., 1999). These two examples serve to illustrate why indicators of 'good' soil structure should include measures related to the architecture of the macropore network, as discussed in Rabot et al. (2018) and Reynolds et al. (2009).

It is well known that soil structure is not static. It is continually changing and evolving at several temporal scales as a result of the influence of various biotic and abiotic factors (Horn, 2004; Horn and Baumgartl, 2002). This is especially the case for arable topsoil which is heavily modified during each growing season by tillage operations (Carter, 1988; Strudley et al., 2008). Soil tillage homogenizes the soil pore network architecture, which then subsequently reverts to a more heterogeneous structure. It is understood that the macropore network in the topmost 10 cm of a freshly harrowed soil exhibits a macro-structure that generally resembles an assortment of soil aggregates of various sizes with a well-connected network of larger pores in between them (Dexter et al., 1983; Jarvis et al., 2017a, 2017b; Schlüter et al., 2018). In this condition, the soil is very well aerated. Infiltrating water is thought to flow more or less homogeneously through the bulk volume of the soil. However, the structure of harrowed soil layers is unstable. After seedbed preparation, the soil starts to consolidate and, in the process, the inter-aggregate pores become smaller and disconnected (Bodner et al., 2013). At the same time, vertically-connected macropores are formed due to root growth and subsequent decay (Angers and Caron, 1998; Bodner et al., 2014), the activity of soil macro-fauna (Jouquet et al., 2006; Wolters, 1991), and the development of shrinkage cracks (Velde, 1999). At higher latitudes, soil structure is also affected by freezing and thawing cycles (Taina et al., 2013). The re-organization of soil structure following tillage operations has consequences for soil

---

functions. For example, water flow becomes more channeled into preferential flow paths, which may lead to increased risks of contaminant leaching (Jarvis, 2007; Jarvis et al., 2016). Moreover, soil regions that are prone to anaerobic conditions become more prevalent, which influences the soil carbon and nitrogen mineralization and the emissions of greenhouse gases such as CO_2, N_2O and CH_4 (Ball, 2013; Ben-Noah and Friedman, 2018).

It has meanwhile been quantitatively established that bulk soil physical properties change with time, e.g. the porosity, the water retention function, the gas and hydraulic conductivities. In contrast, the understanding of the associated evolution of soil structural features is still largely based upon visual inspection of soil profiles and is therefore mostly of a qualitative character. The main reason is that direct quantification of specific pore network properties is aggravated by the opaque nature of soil. Early attempts were undertaken using thin-sections (Dexter, 1976; Dexter et al., 1983; Kwaad and Mucher, 1994). Nowadays 3-D X-ray tomography offers the means to non-destructively image soil pore network architectures in 3-dimensions, whilst also enabling time-lapse imaging of individual soil samples (Cnudde and Boone, 2013; Helliwell et al., 2013). This has been demonstrated in several laboratory experiments to study, for example, the relationship between rainfall-intensity and the development of a surface crust (Augeard et al., 2007), the burrowing of earthworms (Bastardie et al., 2003; Capowiez et al., 2015) and soil-root interactions (Blaser et al., 2018; Tracy et al., 2013).

Time-lapse experiments under natural boundary conditions are needed to thoroughly investigate the interplay between soil structure evolution and its biotic (roots, earthworms, etc.) and abiotic drivers (freezing-thawing cycles, drying-wetting cycles). As mobile X-ray scanners that could be used in-situ, i.e. in the field, will not be available for the foreseeable future, it is necessary to bring the soil samples from the field to the X-ray scanner. A few studies have already included repeated soil sampling at a specific site over longer time-intervals to quantify soil structure evolution using X-ray imaging (e.g. Keller et al., 2017; Sandin et al., 2017). However, the samples in these studies were not re-installed at the field site after X-ray scanning, which necessitated statistical analysis. In these studies, the temporal changes were partially obscured by the large spatial variation in the field. In contrast, re-installing individual soil samples back into the field to enable repeated X-ray imaging of the same sample has the potential to directly provide unambiguous information on how individual processes contribute to the constant re-shaping of soil structure. To our knowledge, such a "litter bag" approach to the study natural soil structure evolution in intact samples, which is common in carbon mineralization studies, has only once before been attempted. The pioneering study of Garbout et al. (2013) focused however on structural evolution of individual selected soil aggregates loosely assembled in microcosms rather than on the evolution of the soil structure as a whole.

In this case study, we aim at demonstrating the potential of time-lapse 3-D X-ray imaging of the evolution of soil structure of one individual soil column installed in a field soil, exposed to natural weather conditions at the surface and connected to the subsoil at its base. Using state-of-the-art X-ray image processing and analyses tools, we discuss the temporal evolution of the soil macropore network architecture with respect to current theories and highlight observations that could lead to new hypotheses that could be tested with similar experimental setups. We also evaluate the future potential applications of the experimental approach presented here as well as some possible limitations.

2. Material and methods

2.1. Sample and site description

An undisturbed soil sample in a PVC cylinder of 10 cm height and 68 mm inner and 76 mm outer diameter (see Fig. 1a) was sampled from the surface soil in a garden plot in Ultuna, approximately three

kilometers south of Uppsala, Sweden (59°49′19.44 N; 17°39′33.49 E), on June 7th, 2013. The climate in Ultuna is characterized as temperate with cold winters and the absence of a dry season (Peel et al., 2007). The average annual temperature and precipitation were 6.5 °C and 549 mm, respectively (1986–2015). Precipitation occurs predominantly in the form of snow in in the winter months. Freezing and thawing events may occur from September to May but are most frequent in early spring, namely March and April. The garden plot had been used for vegetable cultivation since 1977. The soil at the sampling site has been classified as a sandy loam with sand, silt and clay fractions of 0.585, 0.22 and 0.195 $g\,g^{-1}$ (USDA classification). The organic carbon content was 0.022 $kg\,kg^{-1}$.

2.2. Experimental scheme

Prior to the initial soil sampling on June 7th, 2013, the site had been hand plowed to a depth of approximately 10 cm and subsequently harrowed with a rake. Salad rocket (*Eruca sativa*) was sown immediately before the initial sampling. After obtaining the soil sample with help of a hand-held drop-hammer, it was stored in a cold room at approximately 4 °C until a 3-D X-ray image was recorded. The soil sample was subsequently re-installed into the garden plot, with its top surface plane with the surrounding soil surface. Its bottom surface was left open in contact with the soil below. Fig. 1b and c illustrate the soil column as installed in the garden plot (note that both photographs were taken at later stages of this study). The second imaging occasion was on October 20th, 2013. After excavation, the column was immediately scanned with X-ray CT and subsequently re-installed into the garden plot as described above. This procedure was repeated another four times: on March 12th and September 30th in 2014 as well as on March 23rd and July 3rd in 2015, resulting in a time-series of six 3-D X-ray images (Fig. 2). No crops had been sown or planted on the column after its first installation in June 2013.

The air temperature 1.5 m above the soil surface, precipitation and soil temperature at 5 cm depth were recorded daily during the entire experiment at a weather station located approximately 500 m to the south-west of the garden plot. On all 6 imaging occasions, the soil had been draining for at least three days after the last precipitation event. The soil moisture content was therefore assumed to correspond to field capacity or drier.

2.3. Image acquisition

All six X-ray images were acquired using a GE Phoenix v|tome|x 240 industrial X-ray scanner. The X-ray scanner was equipped with a GE 16″ flat panel detector with 2014 × 2014 detector crystals (GE DRX250RT). We adapted the X-ray energy level used for image acquisition to the field-moist bulk density of the soil sample. Due to different water saturation states at the imaging occasions, this resulted in X-ray tube voltages between 140 and 170 kV with electron fluxes between 300 and 570 μA. For each 3-D image, 2000 projections with an isotropic resolution of 65 μm were obtained. The projections were inverted to 3-D images using the GE software datos|x (version 2.1) and exported as TIFF-stacks (tagged image file format) with 16-bit gray-scale resolution.

2.4. Image processing and analyses

2.4.1. Initial registration, gray-scale calibration and filtering

The ImageJ/FIJI (Abramoff et al., 2004; Schindelin et al., 2012) plugin SoilJ (Koestel, 2018) was used to detect the location and orientation of the PVC wall of each column, whereupon the columns were automatically rotated into straight, upright positions and moved into the center of the canvas. Next, an easily trackable stone was selected from within the imaged soil column as a reference landmark. All columns were rotated around their Z-axes until the position of the reference feature in the horizontal plane was identical in all six 3-D

Fig. 1. a) The soil column prior to the X-ray imaging session in March 2015; b) the soil column installed in the garden plot in April 2015; c) the installed soil column in July 2015 (within the base of the tripod) and the Jerusalem artichoke plants growing nearby.

images. This was based upon visual inspection. The subsequently investigated soil consisted of a 60.5 mm tall column, with 48.6 mm of soil above and 11.9 mm below the reference feature for all six individual images. The soil surface was defined as the topmost horizontal cross-section for which the soil matrix occupied 50% of the area inside the column. The uppermost horizontal voxel layer corresponded approximately to the location of the soil surface on the first three imaging locations (June 2013, October 2013 and March 2014). Thereafter, the soil surface was located above the uppermost image layer of the investigated soil volume.

SoilJ was used to calibrate all six images to the same gray-scale. As also done by Hellner et al. (2018), we used the 0.1 percentile gray-value within each horizontal image cross-section as a reference value for air and the median gray-value of the column wall as a reference value for PVC. The calibrated images were then filtered with a 3-D median filter with a radius of 2 voxels in all directions.

2.4.2. Segmentation for morphology analyses

We used the calibrated and median-filtered gray-scale images in full image resolution for morphology analyses. Fig. 3 gives an overview of all image processing and analyses steps carried out in this study. A 3D watershed segmentation was carried out using the MorphoLibJ ImageJ plugin (Legland et al., 2016) with three material classes, namely air,

POM (particulate organic matter, including living roots and soil macro-fauna) and everything denser, i.e. soil matrix as well as sand and gravel. The method required various input information (gray arrows on the left hand side of Fig. 3). First, the gray-scale gradients of the calibrated images obtained with the ImageJ plugin FeatureJ (Meijering, 2015) were used to delineate material edges that serve as watershed boundaries. Second, the region growing algorithm that fills the watersheds is initiated from individual seed regions for each material class. These seed regions were defined based on the joint 2-D histogram of all six X-ray images (Fig. 4), which bins the image voxels not only according to their gray-scale values, but also to their gradients. The seed–region for the POM was delineated by carrying out a separate 2-D watershed algorithm on the 2-D histogram using the frequency peak corresponding to POM as a seed region. The seed region for the 3-D watershed segmentation for the air phase was set to voxels with a gray-value smaller than the largest gradient values of the histogram region pertaining to the POM phase (the left-hand dashed red line in Fig. 4). The seed region for the soil matrix including sand and gravel grains was set to the largest gray-value within the POM seed voxels (the right-hand dashed red line in Fig. 4). All unassigned voxels that do not belong to these seed regions were then filled by a region growing processes that is guided by the 3D gradient image.

The segmented images for the morphology analyses retained a
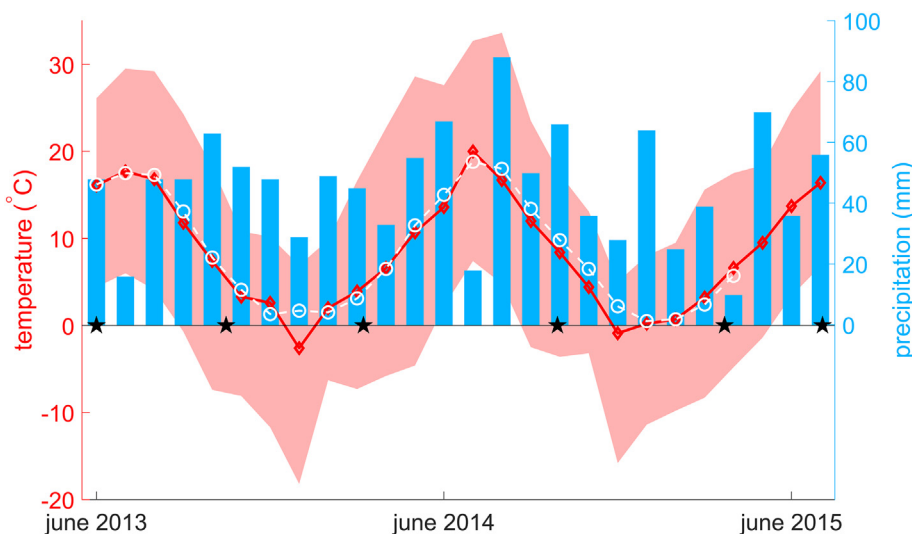
Fig. 2. The monthly mean air temperature and the monthly precipitation in Ultuna during the experiment. The area marked in red indicates minimum and maximal daily values. The dashed white line shows the soil temperature at 5 cm depth. The black stars mark the six days on which the column was taken to the X-ray device for imaging. (For interpretation of the references to colour in this figure legend, the reader is referred to the web version of this article.)
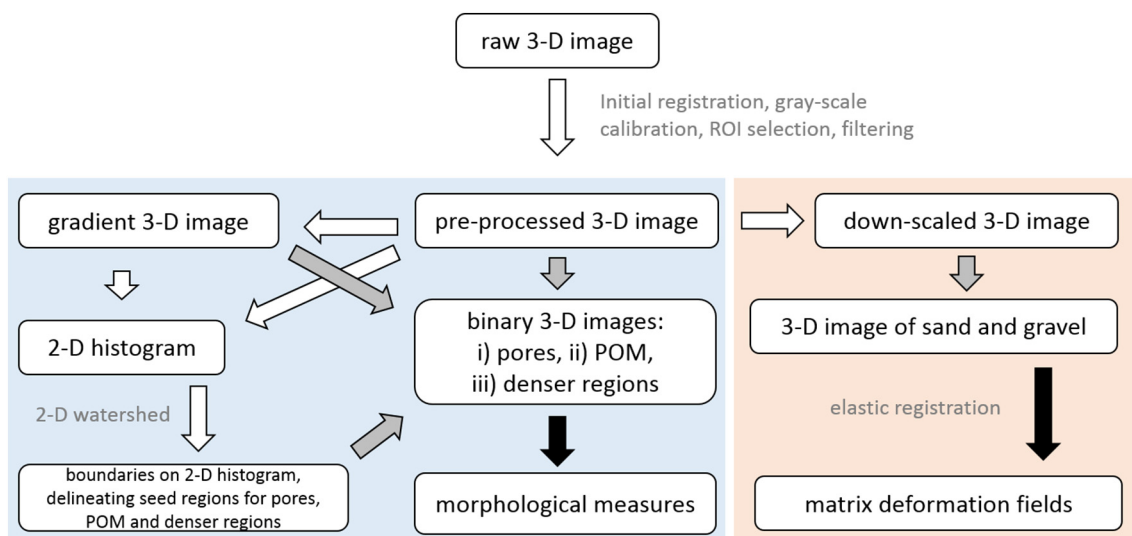
Fig. 3. Workflow illustrating the image processing and analyses steps undertaken in this study. White arrows indicate preprocessing steps, gray arrows segmentation steps and black arrows image analyses.
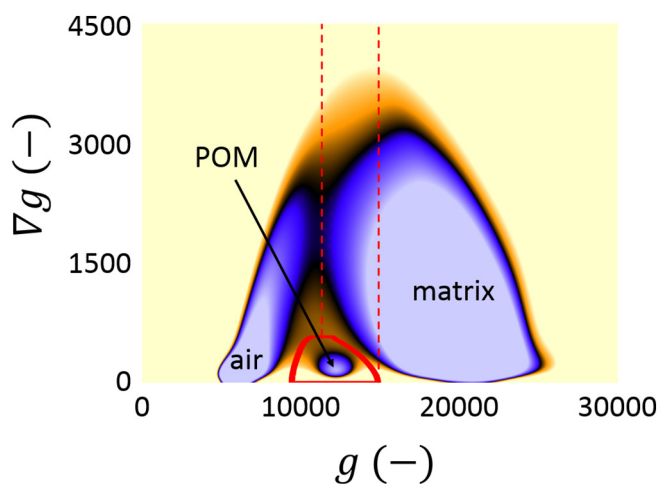
Fig. 4. 2-D joint histogram of all six X-ray images where g denotes the gray-values and ∇ g the gray-value gradients. The colour code depicts the frequency of voxels with respective gray-value and gradient combination where light blue colors indicate large numbers and beige zero entries. The region encircled with a thick red line demarcates the properties of the POM seed voxels used for the watershed segmentation. The seed voxels for air and matrix (and denser) have gray-values and gradients corresponding to the values to the left and the right of the respective dashed red lines. The voxels characterized by the area in between the dashed lines are assigned to either air, POM or matrix phases in the watershed segmentation run on the calibrated gradient images. (For interpretation of the references to colour in this figure legend, the reader is referred to the web version of this article.)

nominal resolution of 65 μm, which gave a feature detection limit of approximately 130 μm. This coincides with the diameter at which macropores are commonly defined (Jarvis, 2007; SSSA, 2008). We will therefore denote the image resolvable pores as macropores in the following. Visualizations of the segmented macropore and POM phases were achieved with Drishti (Limaye, 2012).

2.4.3. Analyses of morphology

We analyzed the morphology of the visible pore space for a central region of interest (ROI) which was 60.5 mm in height and 61.5 mm in diameter, and where 3.3 mm of soil was cut away from the column walls to exclude artificial pores located in the vicinity of the wall.

We used SoilJ (version 1.1.17) for calculating the morphological measures, which involved standard ImageJ routines as well as the fast particle analyzer from BoneJ (Doube et al., 2010). Apart from the soil macroporosity ϕ (mm^3 mm^{-3}) and specific surface area σ (mm^2 mm^{-3}) of the soil pore space, we also computed the following three connectivity measures: the connection probability Γ (−), as defined in Renard and Allard (2013), the percolating soil macroporosity ϕ_p and the critical pore diameter d_c (mm). The connection probability was determined from the imaged pore space by

$$\Gamma = \frac{\sum_{i=1}^{N} n_i^2}{\left(\sum_{i=1}^{N} n_i\right)^2} \tag{1}$$

where N is the number of connected pore clusters, and n_i is the number of pore voxels in cluster i. When all pore voxels in an investigated domain are connected to each other, Γ takes on a value of 1. The more fragmented the pore space gets, the smaller Γ becomes. The percolating porosity ϕ_p corresponds to the volume of all pore voxels contained in all pore clusters that are connected to both, top and bottom of the investigated ROI. The critical pore diameter d_c is defined as the bottleneck in the pore connection from top to bottom. It corresponds to the diameter of the largest sphere that could be moved from top to bottom through the pore system.

Moreover, we calculated the pore size distribution of the visible pores using the maximum inscribed sphere method ('Local Thickness') as implemented in SoilJ. We also computed the distribution of the distance s (mm) to the nearest image resolvable pore with connection to the top of the ROI. Distance s was defined by a 3-D Euclidean distance transform on the volume not segmented as pores in the investigated ROI. Distance s approximates the minimum diffusion path-length that a molecule needs to traverse to reach a location in the soil matrix from the nearest connected macropore.

The soil macroporosity ϕ, the percolating soil macroporosity ϕ_p and the critical pore diameter d_c are known to be positively correlated with saturated hydraulic conductivity, both empirically and according to percolation theory (Katz and Thompson, 1987; Messing and Jarvis, 1990; Koestel et al., 2019). The macroporosities ϕ and ϕ_p as well as the connection probability Γ, the specific macropore surface σ and the distance to the next macropore with surface connection s are correlated with soil aeration. Larger ϕ, ϕ_p and Γ are lead to larger advective and diffusive gas exchanges (Ben-Noah and Friedman, 2018; Kuang et al., 2013). The macropores are the regions within the soil that are vented first with atmospheric air after a period of water saturation. Larger interface surfaces σ between matrix and macropore domains favor the
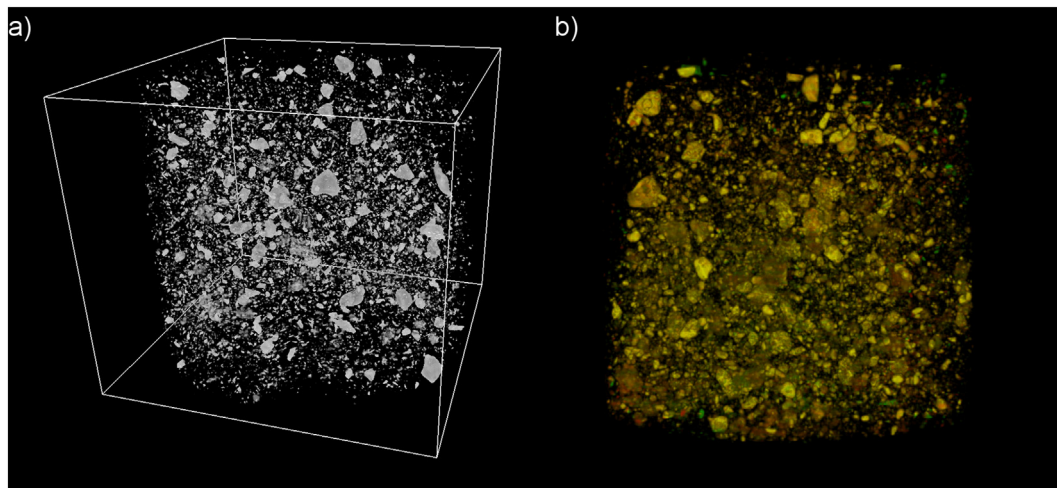
Fig. 5. (a) An example of the sand grains and gravel particles that were used for the matrix deformation quantification. The 3-D image shows the location of the grains in spring 2014. (b) The overlay image between the location of the sand and gravel grains in autumn 2014 shown in green and the registered image from spring 2014 shown in red. The grains are shown in yellow (the result of the additive mixing of red and green) when the elastic registration process was successful. Red and green colors indicate grains that were not successfully tracked. (For interpretation of the references to colour in this figure legend, the reader is referred to the web version of this article.)
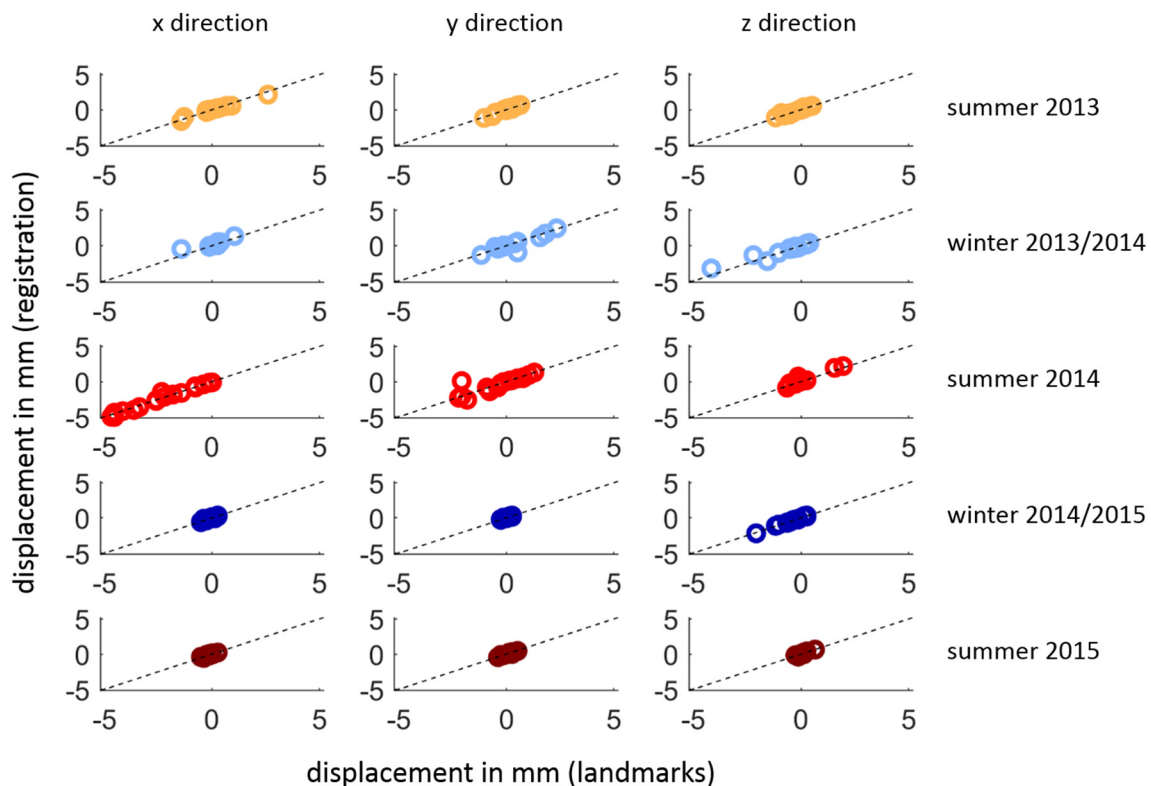
Fig. 6. Validation for the elastic image registration. The x-axes show the displacement of 17 visually detected landmarks between two consecutive X-ray images. The y-axes show the respective displacement at the landmark location as reconstructed by the image registration with Elastix.

diffusive gas exchange between the two and hence contribute by trend to a better soil aeration. Finally, the diffusion path-length s is related to the occurrence and extent of anaerobic microsites (Keiluweit et al., 2018; Sexstone et al., 1985). For the image phase pertaining to POM we restricted ourselves to determining the volume fraction ϕ_{POM} ($mm^3\,mm^{-3}$) and specific surface area σ_{POM} ($mm^2\,mm^{-3}$).

2.4.4. Quantification of soil matrix deformation

2.4.4.1. Image segmentation. We quantified deformation of the soil matrix in the two years of the experiment following the digital

volume correlation approach (Schlüter et al., 2016). The workflow of the matrix deformation quantification is illustrated on the right side of Fig. 3. In short, the rationale is to conduct image registration of a deformed soil onto the previous state with elastic registration and derive the deformation field from the resulting transformation matrix. For this task, we first reduced the image resolution by a factor two (to 130 μm) to save computation time. We then re-scaled the image gray-values so that all pore, particulate organic matter (POM, including living roots) and soil matrix voxels were set to zero and the sand and gravel were displayed with an optimal contrast. This was achieved in

Table 1
The root mean squared errors (RMSE) in mm between the visually detected landmark displacement and the results of the elastic image registration.

	RMSE (mm)		
	x-Direction	y-Direction	z-Direction
Summer 2013	0.18	0.11	0.14
Winter 2013/2014	0.26	0.39	0.36
Summer 2013	0.29	0.59	0.26
Winter 2014/2015	0.11	0.08	0.07
Summer 2013	0.10	0.10	0.09

two steps. First, we set all image regions with densities less than the PVC of the column wall to zero and re-scaled the image gray-values so that minimum and maximum gray-values within each individual image corresponded to the full range available for 16-bit images, i.e. 0 and 65,535. Next, we set all voxels with values smaller than 30,000 to zero in an additional thresholding round. This threshold was obtained upon visual inspection and was suitable to single out sand and gravel from the images. Fig. 5a shows an example image of the sand and gravel grains used for quantifying the soil matrix deformation. The images were then converted to 8-bit, scaling all values larger than 0 to the entire available gray-scale.

2.4.4.2. Elastic registration. The internal displacements of the sand and gravel grains were recovered by elastic image registration of five deformed images acquired during the long-term trial onto the target
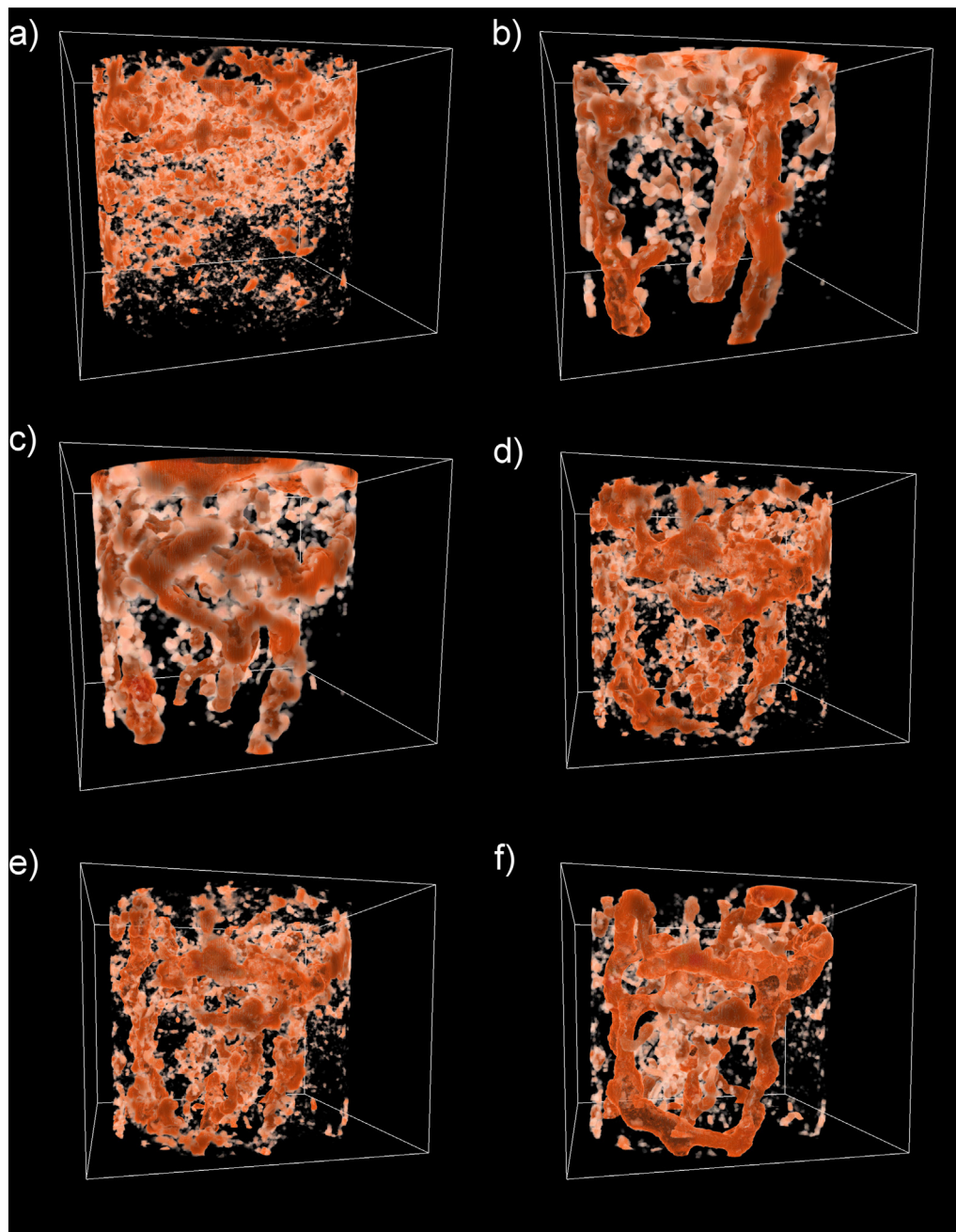
Fig. 7. Evolution of the macropore network structure at the six sampling days: (a) June 7th 2013; (b) October 20th 2013; (c) March 12th 2014, (d) September 30th 2014, (e) March 23rd 2015 and (f) July 3rd 2015.
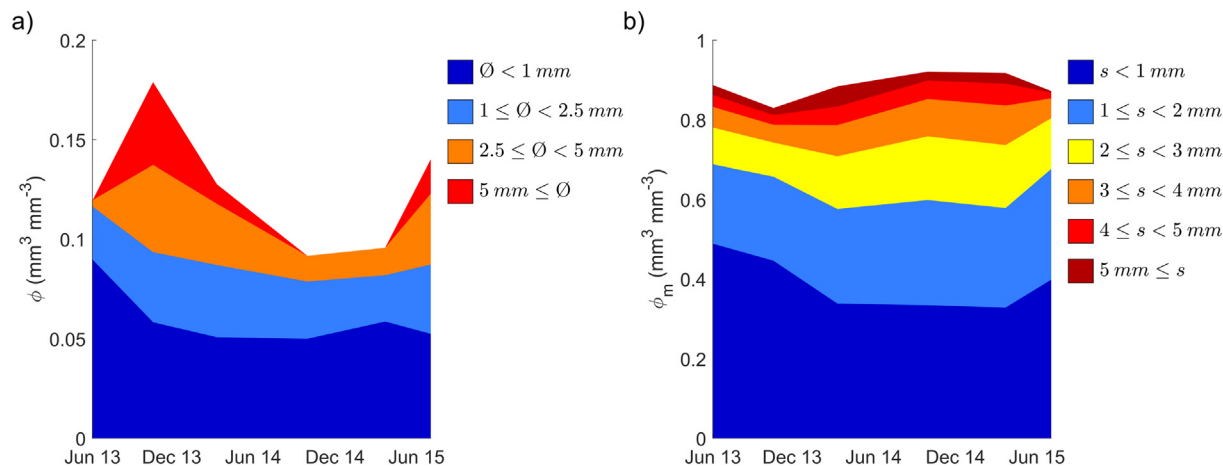
Fig. 8. (a) Evolution of the macroporosity and macropore size distribution and (b) the evolution of the fraction of regions with different distances to the next macropore with connection to the soil surface. The fractions are shown relative to the bulk volume of the investigated region of interest.

image acquired at the previous imaging occasion using the Elastix toolbox (Klein et al., 2010; Shamonin et al., 2014). Spatial alignment was achieved with a B-spline transform that iteratively minimized the mutual information criterion (Mattes et al., 2001) of co-localized voxels in both images. Convergence was accelerated with a four-stage pyramid schedule with resolution reductions by factors of 16, 8, 4 and 2, respectively, which led to a quick alignment at a coarse scale and an iterative refinement at the next finer scale. A smoothness penalty term called 'bending energy' (Klein et al., 2010) was used to constrain the B-spline transform, whereas the regularization weights were determined in a trial and error approach based on expert judgement. A final parameter set was selected for which the location of the registered sand and gravel grains matched sufficiently well with their respective position in the target image, while keeping the bending energy constraint at a maximum. This was done upon visual inspection of overlay images between target and registered image. A 3-D rendering of such an overlay image is shown in Fig. 5b as an example. Identical parameter sets were used for all elastic image registrations carried out in this study.

2.4.4.3. Validation of the elastic registration results. We performed an objective validation of the Elastix results by analyzing the separation distance between the coordinates of 17 landmark features in the target image and the registered image. The 17 landmark features, i.e. easily identifiable sand grains were selected in the X-ray images depicting the sand and gravel phase, covering the investigated ROI as representatively as possible (see Fig. 5a as an illustration of the ROI). The 17 landmarks were traced by visual inspection in all 6 X-ray images. A comparison between the Euclidean displacement obtained from visual inspection and the displacement vector from the elastic registration at the respective coordinates served as the validation. Note that the 17 landmarks were not used to constrain the objective function in Elastix. They were merely used as a metric to validate the registration accuracy.

2.4.4.4. Analyses of the matrix deformation. The displacement of the soil matrix was calculated relative to the previous image. We used this displacement as a proxy for the local deformation of the soil matrix. We note that this approximation is only valid if the sand and gravel grains remain sufficiently stationary relative to soil matrix surrounding them. Assuming that this prerequisite was met, we refer to the displacement of the sand and gravel grains as 'matrix deformation' in the following.

The mean horizontal and vertical matrix deformations δ_{xy} (mm) and δ_z (mm) per soil depth were subsequently analyzed where

$$\delta_{xy} = \sqrt{\delta_x^2 + \delta_y^2} \tag{2}$$

with δ_x and δ_y being the mean horizontal displacement in x and y direction, respectively. δ_{xy} is always positive by definition. In contrast, positive values of δ_z at a specific depth indicate that this soil layer was located at larger heights as compared to the sampling occasion before. Negative δ_z indicate the opposite, namely that the respective layer had lost height relative to the reference object.

In addition we also quantified the mean vertical compaction which is defined as

$$C_z = \frac{d\delta_z}{dz}. \tag{3}$$

The matrix deformations δ_{xy} and δ_z represent displacements of sand grains, the vertical compaction C_z (mm mm^{-1}) quantifies whether the vertical distance between the traced sand grains decreased or increased, corresponding to compaction (positive values) and expansion (negative values). Note that a positive compaction is not necessarily correlated with the image-resolvable pores. Instead, the decrease in porosity that is associated with compaction may be restricted to pores that are smaller than the feature detection limit in the images used in deformation analyses, i.e. smaller than approximately 250 μm. ParaView (Ahrens et al., 2005) was used to visualize the displacement fields.

3. Results

3.1. Validation of the elastic registration

The results of the validation of the elastic registration show that Elastix mimics reasonably well the displacement of the individually selected landmarks (Fig. 6). Table 1 shows that the root mean squared errors (RMSE) between the visually detected landmark displacement and the elastic image registration results ranged between 0.07 and 0.59 mm with a median of 0.14 mm. The latter corresponds approximately to the double of the image resolution, which is in the range of the error expected for the visual detection of the landmarks in the 3-D images. We therefore deduce that the elastic registration is adequate for a quantitative interpretation as it tracked the displacement of sand and gravel grains to a high detail.

3.2. Soil structure evolution

The soil structure after seedbed preparation in June 2013 resembled an assembly of differently sized soil aggregates. The inter-aggregate macropores were relatively homogeneously distributed in the horizontal direction, but the macroporosity declined with depth (Fig. 7a).

a)

b)

c)

d)

e)

f)
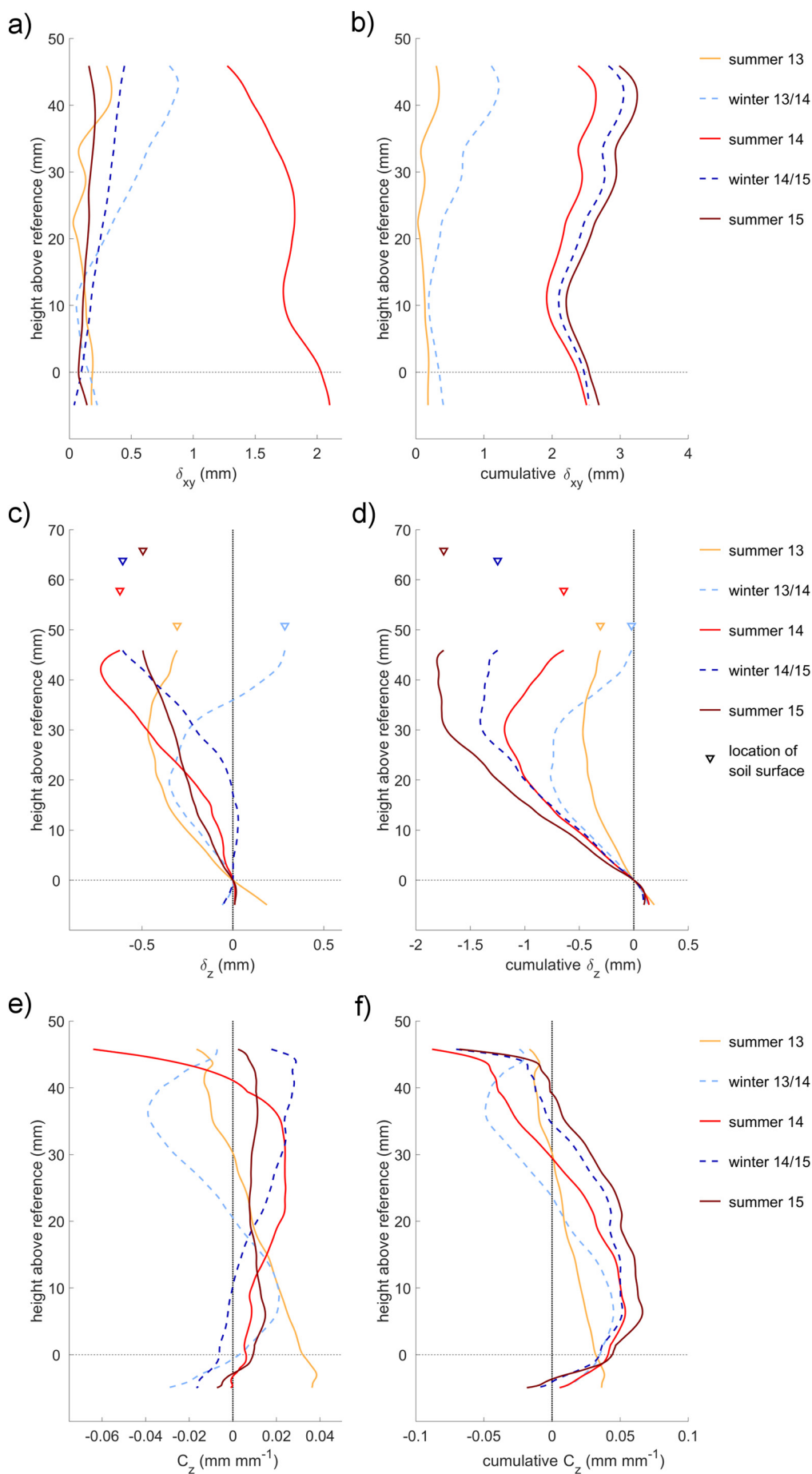
Fig. 9. The mean lateral (δ_{xy}; a and b) and vertical (δ_z; c and d) displacement of the soil matrix between the six sampling occasions. In addition, the vertical compaction C_z, i.e. the derivative of the vertical displacement with depth is shown in e and f. Figures a, c and e depict the displacements and compaction relative to the previous imaging occasion. Figures b, d and f show the cumulative displacement and compaction relative to the image taken on June 15th 2013. To improve readability, the profile lines of the vertical compaction figures were smoothed by a moving average filter with a footprint of 13 mm. Note that the location of the soil surface above the reference object corresponds to the latter of each two sampling occasions for which the displacement and compaction were calculated. The initial location of the soil surface in June 2013 was approximately 50 mm above the reference object.
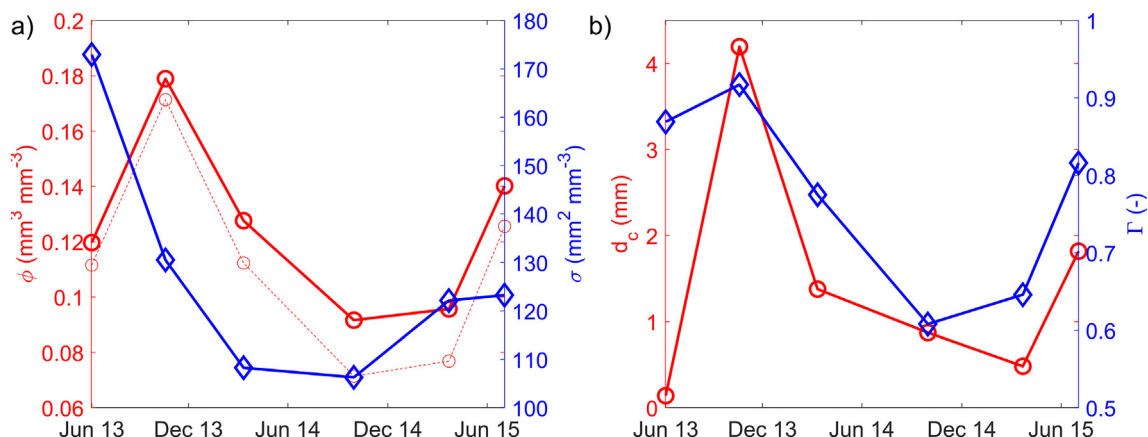
Fig. 10. (a) The evolution of the porosity ϕ (red line and circles) and the specific surface area σ (blue line and diamonds). In addition, the percolating porosity ϕ_p is shown as a dashed line. (b) The evolution of the connectivity measures d_c (critical pore diameter, red line and circles) and Γ (connection probability, blue line and diamonds). (For interpretation of the references to colour in this figure legend, the reader is referred to the web version of this article.)

Clusters of larger macropores were organized in horizontal layers.

This structure was thoroughly modified by faunal burrowing activity until October 2013 (Fig. 7b), which created macropores with diameters larger than 2.5 mm (Fig. 8a). At the same time approximately one third of the volume occupied by macropores with diameters smaller than 1 mm disappeared (Fig. 8a). The net horizontal displacement of sand grains and gravels remained localized and was approximately 0.2 mm throughout the investigated profile (Fig. 9a). Vertical compaction was observed from a depth of 20 mm and below, i.e. in the 30 mm above the reference feature (Fig. 9c and e). Above this depth, the ensemble of traceable sand and gravel grains was slightly expanded. The surface area of the macropores strongly decreased (Fig. 10a), as expected as a consequence of the observed replacement of small by larger macropores (Fig. 8a). All connectivity metrics increased (Fig. 10b), the critical pore diameter d_c by more than an order of magnitude.

By the next imaging occasion in March 2014, the column had been lifted out of the soil by 30 mm (Fig. 5c), probably due to frost heave related to freezing and thawing periods in winter. After X-ray scanning, the column was gently pushed back into the soil after re-installment into the field. The faunal burrowing network inside the soil column had extended somewhat compared to the autumn before. In particular, horizontal galleries had been added, approximately 30 mm above the reference feature (Fig. 7c). At this height, the horizontal displacement of soil tracer particles had also approximately tripled (Fig. 9a). However, some of the burrows had partially refilled and the fraction of large macropores (ø > 5 mm) had strongly decreased (Fig. 9a), as had the overall macroporosity (Fig. 10a). Vertical compaction continued below a depth of 30 mm, whereas above this depth the traced sand and gravel grains indicated that further stretching had occurred (Fig. 9c and e). The soil volume located > 2 mm away from the nearest macropore with a surface connection reached a plateau value of approximately $0.3\,m^3\,m^{-3}$ (Fig. 8b), while it had been $0.2\,m^3\,m^{-3}$ after seedbed preparation. The macropore surface area (Fig. 10a) and all connectivity measures decreased (Fig. 10b).

During the summer of 2014, the tap root of a dandelion (Taraxacum officinale) that had established in 2013 increased greatly in diameter and laterally compressed the soil (Fig. 11c and d), on average by between 1.5 and 2 mm (Fig. 9a). The growth of the dandelion root deformed the entire investigated soil volume, not just the regions next to the root (Fig. 12). Vertical compaction, as indicated by the movement of sand and gravel particles, now occurred over almost the entire investigated volume, which at this same time had sunk to 0.7 mm below the soil surface (Fig. 9c). Only a few fresh macro-faunal burrows were dug sporadically after March 2014 until the following summer (Fig. 7). As a result, macropores with diameters > 2.5 mm become scarce

(Fig. 8a), and the macroporosity ϕ and surface area σ reached their minimum values for the investigated period (Fig. 10a). All the connectivity measures were also at or close to their minimum values (Fig. 10b). During the same period, the POM volume increased by a factor of 7 due to the presence of the large root (Fig. 13).

Over the next winter, the dandelion taproot started to decompose (Fig. 11) and the POM surface area reached a maximum (Fig. 13a). The morphological measures of the macropore space remained at small values. Horizontal matrix deformations were moderate, with stronger deformations in the upper half of the investigated soil volume (Fig. 9a). Vertical compaction was restricted to regions located 20 mm and more above the reference feature, which had by now sunk even deeper below the soil surface (Fig. 9c and e).

During early summer 2015, red ants nested inside the soil column, which was obvious upon visual inspection. Their appearance coincided with smooth-walled and well inter-connected macropores that roughly followed the formerly partially refilled old biopore network (Fig. 7f). At the same time, the decay of the dandelion root continued (Fig. 11f, Fig. 13). During this period, macroporosity clearly increased and macropores with diameters > 2.5 mm once again became more abundant (Fig. 8a). The distance to the next macropore with surface connection also decreased markedly (Fig. 8b) while macropore network connectivity increased (Fig. 10b). The horizontal matrix deformation was small and similar to that observed during the vegetation period of 2013, with vertical compaction of the traceable sand and gravel grains taking place uniformly across the investigated ROI (Fig. 9).

4. Discussion

The evolution of soil structure during the first growing season followed the expected development after tillage and seedbed preparation that had been discussed in the introduction of this paper. In short, the loose aggregate structure was consolidated by settling and wetting and drying cycles and biopores were dug by soil macro-fauna. Judging from their size and characteristics, the biopores were most likely created by earthworms (Astrid Taylor, personal communication). The vertical compaction during the summer 2013 of the soil was restricted to 20+ mm below the soil surface (Fig. 9f) and only affected pores with diameters < 1 mm (Fig. 7a). During the same period, the soil macroporosity increased to over 20 vol%, where one third of this corresponded to biopores with diameters larger than 2.5 mm (Fig. 7a). As a result, the critical pore diameter d_c increased by more than an order of magnitude from 0.14 to 4.2 mm during the first summer, corresponding to the smallest and largest observed values during the entire experiment. According to percolation theory (Katz and Thompson, 1987), this suggests an increase of saturated hydraulic conductivity by a factor of
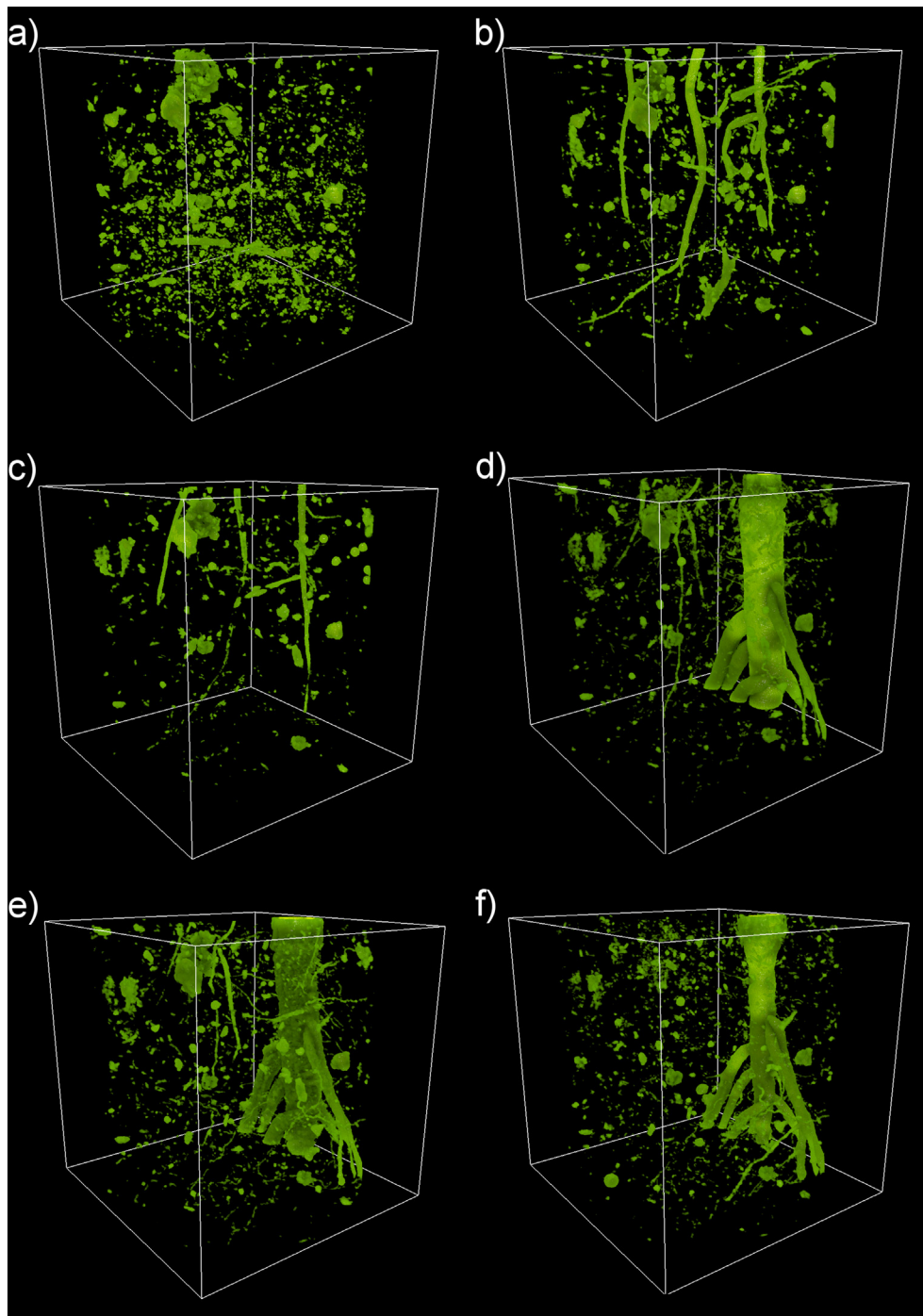
Fig. 11. Image resolvable POM on the six sampling days: (a) June 15th 2013; (b) October 20th 2013; (c) March 12th 2014, (d) September 30th 2014, (e) March 23rd 2015 and (f) July 3rd 2015.

approximately 900 in the ROI volume within a few months, as the theory postulates a proportionality between saturated hydraulic conductivity and the square of the critical pore diameter. The very large variation in critical pore diameter d_c is hence in line with previous observations that show that saturated hydraulic conductivity is temporally highly variable (e.g. Messing and Jarvis, 1990; Strudley et al., 2008; Schwen et al., 2011).

The macropore connectivity probability Γ increased from an already high initial level after seedbed preparation in summer 2013 to a maximum value of > 0.9 in autumn 2013. However, the concomitant decrease of the macropore surface area σ (Fig. 10a) and the increase of the average distance s indicated a slight worsening of the soil matrix

aeration conditions approximated by the distribution of macropore distances (Fig. 8b). Minimum values for σ and s were reached at the subsequent imaging sessions (Figs. 8b and 10a). Γ decreased even further to its minimum value of 0.61 in autumn 2014, after the dandelion root had strongly increased in diameter (Fig. 11) and shifted soil particles in the entire soil column (Fig. 12). The morphological indicators relevant for a good soil aeration only improved again when the dandelion root started to decay over winter 2014/2015 and when red ants had built a burrow in summer 2015. Note that this is only a very general inference as it does not take local living condition for oxygen consuming microorganisms into account, which may strongly influence the distribution of anoxic regions in a soil volume (Keiluweit et al., 2018).
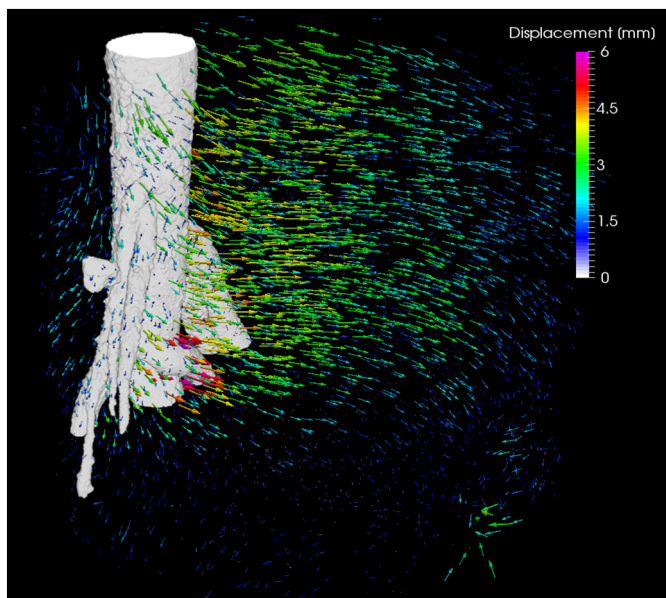
Fig. 12. Soil matrix displacement field caused by the growth of the dandelion tap root (shown in white) in autumn 2014. The displacement vectors stem from the Elastix image registration.
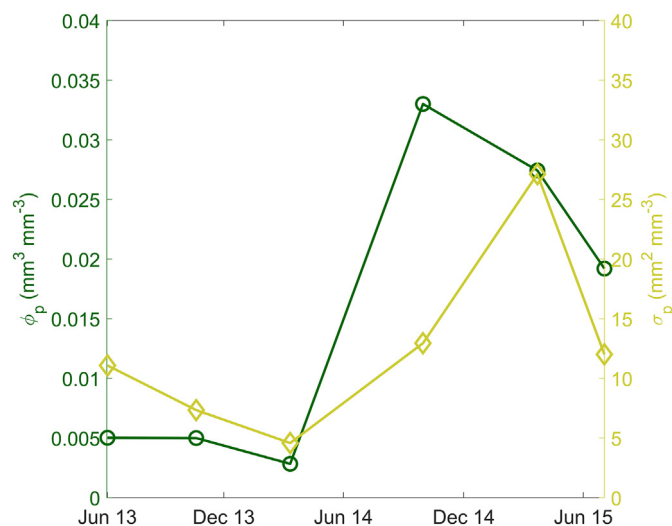
Fig. 13. The evolution of POM volume fraction ϕ_{POM} and specific surface area σ_{POM}.

Such a comprehensive assessment of the 3D distribution of microbial activity in natural soil was technically not feasible within the scope of this study.

It is striking that macropores with diameters larger than 5 mm, to which the critical pore diameter d_c was positively correlated, were short-lived. Their existence appeared to be closely connected to increased burrowing activity of the soil macro-fauna, as during the summers of 2013 and 2015 (Figs. 7 and 8a). The volume fraction of macropores with diameters between 2.5 and 5 mm varied less much, but was still positively related to burrowing activity and decreased during summer 2014, when the dandelion root strongly increased in diameter (Fig. 11). In contrast, the volume fraction of macropores with diameters between 1 and 2 mm remained surprisingly constant on all six imaging occasions. The volume fraction of the smallest image-resolvable pores also remained reasonably constant once it had dropped to values of ca. $0.05 \, \text{cm}^3 \, \text{cm}^{-3}$ after seedbed preparation. In future research, it may be worthwhile to investigate whether the stability of

these volume fractions was observed by chance or whether it is related to self-organizing biological processes that keep the volume fraction of these pore size classes at optimum values for the functioning of the local soil ecosystem, similar to what is discussed in Lavelle et al. (2016).

Bioturbation was a very important driver of soil macrostructure dynamics in this study. Together with the tillage at the start of the field experiment, the burrowing activity of soil macro-fauna appeared to be one main driver, creating a well-aerated network of larger macropores, but also some compression of smaller pores (Schrader et al., 2007). The growth of the dandelion taproot acted in only one direction, causing compression. Only after a longer time period, i.e. after its complete decay, the space formerly occupied by the tap root may be converted to larger biopores. Quantification of the soil deformation field revealed that burrowing macro-fauna in soil clearly had a much more localized impact on the surrounding soil structure than the lateral growth of the dandelion tap-root (Fig. 9a and b). Both led to predominantly lateral compaction of the soil matrix, but that observed as a result of the growth of the dandelion root exceeded that caused by the burrowing activity by a factor of 10 (Fig. 9a).

Vertical soil compaction continued during the entire observation period, but was initially constrained to soil at > 20 mm depth, i.e. 30 mm or less above the reference object (Fig. 9c, d, e and f). During the winter of 2013/2014, the uppermost 20 mm of the soil was even expanding. The latter was observed simultaneously with the ejection of the PVC column out of the soil by 30 mm during this winter, most probably as a consequence of frost heave in the uppermost soil layers. The movement of the PVC column may have been caused by the growth of needle ice or to soil redistribution during freezing and thawing. The vertical expansion of the uppermost soil layers may have been caused by the freezing and thawing directly or as a co-transport with the upwards movement of the PVC column.

With this study, we wished to demonstrate the feasibility of the methodologies ("proof-of-concept"), quantifying the evolution of soil structure on one sample by repeated X-ray imaging. It is obvious that the value of future experiments will be greatly increased by using replicate samples, allowing the separation of average trends from outliers. In this fashion, the structure resulting from specific management practices could be quantified, for example its evolution following different tillage operations or the introduction of new crops. By extracting soil macro-fauna and lining the soil samples with fine nylon gauze to prevent re-colonization, the impact of their burrowing activity could be quantified and separated from other biotic factors. By using herbicides, experimental setups that evaluate root-related contributions to soil structure formation are feasible. Such kind of data could also prove very useful for constructing and testing 'next-generation' models that link a dynamic description of soil structure to various processes and functions in the soil-plant system.

The experimental setup may be improved by using columns with holes or a mesh-like column material as it was done by Garbout et al. (2013). This would allow roots and fauna to enter and leave the column in the horizontal directions. It would also partly remove the artificial barrier to lateral soil displacement that the solid PVC column wall posed in our study. A mesh at the bottom could prevent lifting of the soil column out of the soil, as observed in this study. When re-installing columns in the field, it is important to preserve a similar bulk density at the interface between column and surrounding soil so as not to artificially create barriers for roots and soil life. Measurements of the soil matric potential and water content in the vicinity of the soil columns would also be very useful, as it would allow relating volume changes of the soil matrix, for example due to swelling and shrinking, to the water saturation state at the time of imaging. Moreover, this would enable a quantitative interpretation of the gray values and density of the soil matrix. Future experiments should also investigate the impact of repeated soil sampling and re-installation on soil structure evolution, root growth and faunal activity. This could be achieved by comparing repeatedly excavated samples with samples that remained buried for the

entire period.

5. Conclusions

This experimental setup described here enables a detailed and explicit quantification of in-situ soil structure dynamics at the small column scale. We see a large potential for studies with similar setups, in which replicated samples are used to quantify the contributions of individual processes driving soil structural evolution in the short and long-term, which in turn modifies associated soil functions like aeration and water flow that are important for crop production and organic carbon and nutrient cycling. In this fashion, the structure evolution following different soil tillage operations or the effects of different crops could also be investigated.

In addition, the case study also raised attention to specific processes that may be evaluated in follow up studies, which should involve replicate samples. Among these are investigations on the relationship between critical pore diameter and air and water conductivity, evaluations of volumes of compaction resulting from macro-faunal burrowing activities and root growth, the longevity of macropores, especially large ones, and whether equilibrium states exist for morphological measures of soil structure.

Acknowledgement

References

Abramoff, M.D., Magalhaes, P.J., Ram, S.J., 2004. Image processing with ImageJ. Biophoton. Int. 11, 36–42.

Ahrens, J., Geveci, B., Law, C., 2005. ParaView: an end-user tool for large data visualization. In: Visualization Handbook. Elsevier.

Angers, D.A., Caron, J., 1998. Plant-induced changes in soil structure: processes and feedbacks. Biogeochemistry 42 (1–2), 55–72.

Assouline, S., 2013. Infiltration into soils: conceptual approaches and solutions. Water Resour. Res. 49 (4), 1755–1772.

Augeard, B., Assouline, S., Fonty, A., Kao, C., Vauclin, M., 2007. Estimating hydraulic properties of rainfall-induced soil surface seals from infiltration experiments and X-ray bulk density measurements. J. Hydrol. 341 (1–2), 12–26.

Ball, B.C., 2013. Soil structure and greenhouse gas emissions: a synthesis of 20 years of experimentation. Eur. J. Soil Sci. 64 (3), 357–373.

Bastardie, F., Capowiez, Y., de Dreuzy, J.R., Cluzeau, D., 2003. X-ray tomographic and hydraulic characterization of burrowing by three earthworm species in repacked soil cores. Appl. Soil Ecol. 24 (1), 3–16.

Ben-Noah, I., Friedman, S.P., 2018. Review and evaluation of root respiration and of natural and agricultural processes of soil aeration. Vadose Zone J. 17 (1).

Blaser, S.R.G.A., Schlüter, S., Vetterlein, D., 2018. How much is too much?—influence of X-ray dose on root growth of faba bean (Vicia faba) and barley (Hordeum vulgare). PLoS One 13 (3), e0193669.

Bodner, G., Scholl, P., Kaul, H.P., 2013. Field quantification of wetting-drying cycles to predict temporal changes of soil pore size distribution. Soil Tillage Res. 133 (1–9).

Bodner, G., Leitner, D., Kaul, H.P., 2014. Coarse and fine root plants affect pore size distributions differently. Plant Soil 380 (1–2), 133–151.

Capowiez, Y., Bottinelli, N., Sammartino, S., Michel, E., Jouquet, P., 2015. Morphological and functional characterisation of the burrow systems of six earthworm species (Lumbricidae). Biol. Fertil. Soils 51 (7), 869–877.

Carter, M.R., 1988. Temporal variability of soil macroporosity in a fine sandy loam under moldboard plowing and direct drilling. Soil Tillage Res. 12 (1), 37–51.

Cnudde, V., Boone, M.N., 2013. High-resolution X-ray computed tomography in geosciences: A review of the current technology and applications. Earth-Sci. Rev. 123, 1–17.

Dexter, A.R., 1976. Internal structure of tilled soil. J. Soil Sci. 27 (3), 267–278.

Dexter, A.R., Radke, J.K., Hewitt, J.S., 1983. Structure of a tilled soil as influenced by tillage, wheat cropping, and rainfall. Soil Sci. Soc. Am. J. 47 (3), 570–575.

Doube, M., Klosowski, M.M., Arganda-Carreras, I., Cordelieres, F.P., Dougherty, R.P., Jackson, J.S., Schmid, B., Hutchinson, J.R., Shefelbine, S.J., 2010. BoneJ free and extensible bone image analysis in ImageJ. Bone 47 (6), 1076–1079.

Garbout, A., Munkholm, L.J., Hansen, S.B., 2013. Temporal dynamics for soil aggregates determined using X-ray CT scanning. Geoderma 204/205, 15–22. https://doi.org/10.1016/j.geoderma.2013.04.004.

Helliwell, J.R., Sturrock, C.J., Grayling, K.M., Tracy, S.R., Flavel, R.J., Young, I.M., Whalley, W.R., Mooney, S.J., 2013. Applications of X-ray computed tomography for examining biophysical interactions and structural development in soil systems: a review. Eur. J. Soil Sci. 64 (3), 279–297.

Hellner, Q., Koestel, J., Ulén, B., Larsbo, M., 2018. Effects of tillage and liming on macropore networks derived from X-ray tomography images of a silty clay soil. Soil Use Manag. 34 (2), 197–205.

Horn, R., 2004. Time dependence of soil mechanical properties and pore functions for arable soils. Soil Sci. Soc. Am. J. 68 (4), 1131–1137.

Horn, R., Baumgartl, T., 2002. Dynamic properties of soils. In: Soil Physics Companion, pp. 17–48.

Jarvis, N.J., 2007. A review of non-equilibrium water flow and solute transport in soil macropores: principles, controlling factors and consequences for water quality. Eur. J. Soil Sci. 58 (3), 523–546.

Jarvis, N., Koestel, J., Larsbo, M., 2016. Understanding preferential flow in the vadose zone: recent advances and future prospects. Vadose Zone J. 15. https://doi.org/10.2136/vzj2016.09.0075.

Jarvis, N., Larsbo, M., Koestel, J., 2017a. Connectivity and percolation of structural pore networks in a cultivated silt loam soil quantified by X-ray tomography. Geoderma 287, 71–79.

Jarvis, N., Forkman, J., Koestel, J., Kätterer, T., Larsbo, M., Taylor, A., 2017b. Long-term effects of grass-clover leys on the structure of a silt loam soil in a cold climate. Agric. Ecosyst. Environ. 247, 319–328. https://doi.org/10.1016/j.agee.2017.06.042.

Jouquet, P., Dauber, J., Lagerlof, J., Lavelle, P., Lepage, M., 2006. Soil invertebrates as ecosystem engineers: intended and accidental effects on soil and feedback loops. Appl. Soil Ecol. 32 (2), 153–164.

Katz, A.J., Thompson, A.H., 1987. Prediction of rock electrical-conductivity from mercury injection measurements. J. Geophys. Res. Solid Earth Planets 92 (B1), 599–607.

Keiluweit, M., Gee, K., Denney, A., Fendorf, S., 2018. Anoxic microsites in upland soils dominantly controlled by clay content. Soil Biol. Biochem. 118, 42–50.

Keller, T., Colombi, T., Ruiz, S., Manalili, M.P., Rek, J., Stadelmann, V., Wunderli, H., Breitenstein, D., Reiser, R., Oberholzer, H., Schymanski, S., Romero-Ruiz, A., Linde, N., Weisskopf, P., Walter, A., Or, D., 2017. Long-term soil structure observatory for monitoring post-compaction evolution of soil structure. Vadose Zone J. 16 (4).

Klein, S., Staring, M., Murphy, K., A Viergever, M., P W Pluim, J., 2010. Elastix: a toolbox for intensity-based medical image registration. IEEE Trans. Med. Imaging 29, 196–205.

Koestel, J., 2018. SoilJ: an ImageJ plugin for the semiautomatic processing of three-dimensional X-ray images of soils. Vadose Zone J. 17 (1).

Koestel, K., Dathe, A., Skaggs, T.H., Klakegg, O., Ahmad, M.A., Babko, M., Gimenez, D., Farkas, C., Nemes, A., Jarvis, N., 2019. Estimating the permeability of naturally-structured soil from percolation theory and pore space characteristics imaged by X-ray. Water Resour. Res. 54. https://doi.org/10.1029/2018WR023609.

Kuang, X.X., Jiao, J.J., Li, H.L., 2013. Review on airflow in unsaturated zones induced by natural forcings. Water Resour. Res. 49 (10), 6137–6165.

Kwaad, F., Mucher, H.J., 1994. Degradation of soil-structure by welding - a micromorphological study. Catena 23 (3–4), 253–268.

Lavelle, P., Spain, A., Blouin, M., Brown, G., Decaens, T., Grimaldi, M., Jose Jimenez, J., McKey, D., Mathieu, J., Velasquez, E., Zangerle, A., 2016. Ecosystem engineers in a self-organized soil: a review of concepts and future research questions. Soil Sci. 181, 91–109. https://doi.org/10.1097/ss.0000000000000155.

Legland, D., Arganda-Carreras, I., Andrey, P., 2016. MorphoLibJ: integrated library and plugins for mathematical morphology with ImageJ. Bioinformatics 32 (22), 3532–3534.

Limaye, A., 2012. Drishti: a volume exploration and presentation tool. In: Stock, S.R. (Ed.), Developments in X-Ray Tomography VIII.

Mattes, D., Haynor, D.R., Vesselle, H., Lewellyn, T.K., Eubank, W., 2001. Nonrigid multimodality image registration. In: Medical Imaging 2001. SPIE, pp. 12.

Meijering, E., 2015. FeatureJ: An ImageJ Plugin Suite for Image Feature Extraction. http://imagescience.org/meijering/software/featurej/.

Messing, I., Jarvis, N.J., 1990. Seasonal variation in field-saturated hydraulic conductivity in two swelling clay soils in Sweden. J. Soil Sci. 41 (2), 229–237.

Parry, S., Renault, P., Chenu, C., Lensi, R., 1999. Denitrification in pasture and cropped soil clods as affected by pore space structure. Soil Biol. Biochem. 31 (4), 493–501.

Peel, M.C., Finlayson, B.L., McMahon, T.A., 2007. Updated world map of the Köppen-Geiger climate classification. Hydrol. Earth Syst. Sci. 11 (5), 1633–1644.

Rabot, E., Wiesmeier, M., Schlüter, S., Vogel, H.J., 2018. Soil structure as an indicator of soil functions: A review. Geoderma 314, 122–137.

Renard, P., Allard, D., 2013. Connectivity metrics for subsurface flow and transport. Adv. Water Resour. 51 (0), 168–196.

Reynolds, W.D., Drury, C.F., Tan, C.S., Fox, C.A., Yang, X.M., 2009. Use of indicators and pore volume-function characteristics to quantify soil physical quality. Geoderma 152 (3–4), 252–263.

Sandin, M., Koestel, J., Jarvis, N., Larsbo, M., 2017. Post-tillage evolution of structural pore space and saturated and near-saturated hydraulic conductivity in a clay loam soil. Soil Tillage Res. 165, 161–168.

Schindelin, J., Arganda-Carreras, I., Frise, E., Kaynig, V., Longair, M., Pietzsch, T., Preibisch, S., Rueden, C., Saalfeld, S., Schmid, B., Tinevez, J.-Y., White, D.J., Hartenstein, V., Eliceiri, K., Tomancak, P., Cardona, A., 2012. Fiji: an open-source platform for biological-image analysis. Nat. Methods 9 (7), 676–682.

Schlüter, S., Leuther, F., Vogler, S., Vogel, H.J., 2016. X-ray microtomography analysis of soil structure deformation caused by centrifugation. Solid Earth 7 (1), 129–140.

Schlüter, S., Großmann, C., Diel, J., Wu, G.-M., Tischer, S., Deubel, A., Rücknagel, J., 2018. Long-term effects of conventional and reduced tillage on soil structure, soil ecological and soil hydraulic properties. Geoderma. https://doi.org/10.1016/j.geoderma.2018.07.001.

Schrader, S., Rogasik, H., Onasch, I., Jegou, D., 2007. Assessment of soil structural differentiation around earthworm burrows by means of X-ray computed tomography and scanning electron microscopy. Geoderma 137, 378–387. https://doi.org/10.1016/j.geoderma.2006.08.030.

Schwen, A., Bodner, G., Scholl, P., Buchan, G.D., Loiskandl, W., 2011. Temporal dynamics of soil hydraulic properties and the water-conducting porosity under different tillage. Soil Tillage Res. 113, 89–98. https://doi.org/10.1016/j.still.2011.02.005.

Sexstone, A.J., Revsbech, N.P., Parkin, T.B., Tiedje, J.M., 1985. Direct measurement of oxygen profiles and denitrification rates in soil aggregates. Soil Sci. Soc. Am. J. 49 (3), 645–651.

Shamonin, D., Bron, E., Lelieveldt, B., Smits, M., Klein, S., Staring, M., 2014. Fast parallel image registration on CPU and GPU for diagnostic classification of Alzheimer's disease. Front. Neuroinform. 7 (50).

SSSA, 2008. Glossary of Soil Science Terms 2008. Soil Science Society of America, Madison, WI.

Strudley, M.W., Green, T.R., Ascough, J.C., 2008. Tillage effects on soil hydraulic properties in space and time: state of the science. Soil Tillage Res. 99 (1), 4–48.

Taina, I.A., Heck, R.J., Deen, W., Ma, E.Y.T., 2013. Quantification of freeze-thaw related structure in cultivated topsoils using X-ray computer tomography. Can. J. Soil Sci. 93 (4), 533–553.

Tracy, S.R., Black, C.R., Roberts, J.A., Mooney, S.J., 2013. Exploring the interacting effect of soil texture and bulk density on root system development in tomato (Solanum lycopersicum L.). Environ. Exp. Bot. 91, 38–47.

Velde, B., 1999. Structure of surface cracks in soil and muds. Geoderma 93 (1–2), 101–124.

Wolters, V., 1991. Soil invertebrates - effects on nutrient turnover and soil structure - a review. Z. Pflanzen. Bodenk. 154 (6), 389–402.